Creative Commons Attribution 4.0 International (CC BY 4.0)
https://creativecommons.org/licenses/by/4.0/

Access to this work was provided by the University of Maryland, Baltimore County (UMBC) ScholarWorks@UMBC digital repository on the Maryland Shared Open Access (MD-SOAR) platform.

Please provide feedback

Please support the ScholarWorks@UMBC repository by emailing scholarworks-group@umbc.edu and telling us what having access to this work means to you and why it's important to you. Thank you.

Research Square

Preprints are preliminary reports that have not undergone peer review.
They should not be considered conclusive, used to inform clinical practice,
or referenced by the media as validated information.

Seismic resurfacing of asteroid (433) Eros from cratering impact suggests presence of asteroid families in near-Earth space

Ronald-Louis Ballouz (ronald.ballouz@jhuapl.edu)
Johns Hopkins University Applied Physics Lab https://orcid.org/0000-0002-1772-1934
Carolyn Ernst
JHUAPL
Olivier Barnouin
Johns Hopkins University Applied Physics Laboratory https://orcid.org/0000-0002-3578-7750
Ronald Daly
Johns Hopkins University Applied Physics Laboratory https://orcid.org/0000-0002-1320-2985
Daniella DellaGiustina
Lunar and Planetary Lab, University of Arizona
Benjamin Hyatt
University of Maryland, Baltimore County
Anna Martin
Johns Hopkins University Applied Physics Lab

Physical Sciences - Article

Keywords:

Posted Date: October 6th, 2022

DOI: https://doi.org/10.21203/rs.3.rs-2133467/v1

License: This work is licensed under a Creative Commons Attribution 4.0 International License.
Read Full License

Title: **Seismic resurfacing of asteroid (433) Eros indicates a recent formation age for Shoemaker crater and the presence of cratering families in near-Earth space**

Authors:
R.-L Ballouz[1*], C.M. Ernst[1*], O.S. Barnouin[1], R.T. Daly[1], D.N. DellaGiustina[2], B.A. Hyatt[3], A.C. Martin[1]

[1]Johns Hopkins University Applied Physics Lab, Laurel, MD, USA
[2]Lunar and Planetary Lab, University of Arizona, Tucson, AZ, USA
[3]University of Maryland, Baltimore County, Baltimore, MD, USA
*These authors contributed equally to this work

Abstract:

An asteroid's interior contributes to the response of its surface and shape to forces from space, including meteoroid impacts [e.g., Chapman 1996, Bottke et al. 2020], tidal effects [e.g., Hurford et al. 2016, Binzel et al. 2010], and solar radiation [Walsh et al. 2008]. Changes to asteroid surfaces from these external forces provide a record of the collisional and dynamical evolution of the inner Solar System [Bottke et al. 2020]. However, asteroid interiors remain poorly understood [Asphaug 2020].

(433) Eros is a 34 km x 11 km x 11 km diameter elongated near-Earth asteroid (NEA) with surface expressions that suggest a heavily fractured yet coherent interior, as evidenced by craters formed with structural control [Prockter et al. 2002] and by surface lineaments [Buczkowski et al. 2008], which are common features on 10-km-scale asteroids observed by spacecraft [Veverka et al. 1994, Barucci et al. 2015] that may be surface expressions of widespread interior fractures.

Here we report on measurements of the degradation of the D > 500 m crater population in the vicinity of the 7.5-km-diameter Shoemaker crater, indicating that seismic surface waves and crater ejecta, rather than seismic body waves [Richardson 2005, Thomas & Robinson 2005], erased craters with D < 500 m only up to 10 km away from the crater center. We use crater degradation measurements to estimate a surface wave seismic diffusivity of 0.02 km^2/s for Eros regolith.

We determine from these observations that 10-100-km scale fractured asteroids strongly attenuate impact-induced seismic surface waves and seismic resurfacing is limited to local regions, less that 3 crater radii from the impact point.

Our results indicate that Shoemaker crater formed 6.5–31.8 Ma, while Eros was in a main-belt resonance zone. The age of Shoemaker crater coincides with the cosmic ray exposure age of some ordinary chondrites and the returned samples from the 0.3-km-diameter, S-type NEA Itokawa [Nagao et al. 2011]. The concurrence of ages suggests that large cratering impacts on to 10-km scale asteroids are an important source of NEAs and meteorites.

Introduction

The Near-Earth Asteroid Rendezvous (NEAR) mission obtained global imaging coverage of the NEA (433) Eros with its Multi-Spectral Imager (MSI). The MSI revealed a regolith-covered surface that is heavily cratered at large scales [Chapman et al., 2002]. Eros has three large impact craters that dominate its shape: Himeros (9.7-km-diameter), Shoemaker[1] (7.5-km-diameter), and Psyche (5.6-km-diameter). Shoemaker is thought to be the youngest of these craters, based on its superposition of Himeros and the distribution of boulders and craters in its vicinity [Robinson et al., 2002]. The distribution of large boulders (> 30 m-diameter) on Eros qualitatively matches modeled patterns of ejecta from the formation of Shoemaker crater [Thomas et al. 2001]. Furthermore, Eros exhibits a global deficiency in small craters [Chapman et al., 2002; Robinson et al., 2002], with craters <200 m depleted relative to predicted empirical saturation. Depletion of small crater populations has also been observed on other NEAs visited by spacecraft such as Itokawa [Hirata et al., 2009], Ryugu [Sugita et al. 2019], and Bennu [Walsh et al. 2019, Bierhaus et al. 2022]. The small sizes of NEAs (all < 20-km-diameter) precludes endogenic processes, such as volcanism, as means of surface modification. Therefore, the observed small crater deficiency implies the existence either of a mechanism that selectively prevents small crater formation, such as impact armoring [Tatsumi & Sugita 2018, Barnouin et al. 2019, Bierhaus et al. 2022], or a process that preferentially erases them, such as impact-induced seismic shaking or ejecta deposition.

Statistical models of the depletion of small craters with diameters $D < 100$ m on Eros suggest that impact-induced seismicity has refreshed its surface [Richardson et al. 2005]. However, it is unclear whether seismic shaking on fractured, 10-km-scale asteroids leads to global [Richardson et al. 2005, 2020, Asphaug 2008] or regional [Thomas & Robinson 2005] resurfacing. To resolve this mystery, we measured the morphology of craters on Eros, and modeled their degradation through ejecta deposition and seismic effects.

Measuring d/D and emergent trends

We measured the depth and diameters of craters (≥240 m in diameter, and complete to 550 m) by creating high-resolution (3-m ground sample distance) digital terrain models (DTMs) using co-registered, high-resolution images from the MSI and a high-resolution stereophotoclinometry (SPC) shape model of the asteroid [Gaskell, 2008]. The accuracy of the DTMs was confirmed by comparison to topographic data from the NEAR Laser Rangefinder (NLR) (see Methods Sec. 1). Crater depth-to-diameter ratios (*d/D*) on Eros had been previously reported through shadow measurements [Robinson et al. 2002] and using NLR profiles [Marchi et al. 2015]; both approaches relied on simplifying assumptions and the level of completeness of that survey is unclear. Robinson et al. [2002] assumed a nominal parabolic crater shape to infer the depth of the craters. The NLR technique [Marchi et al. 2015] used individual transects that best cut through the middle of a crater. Both of these techniques suffer from using just one measurement of depth per crater. The shadow-measurement approach assumes regional variations in topography are well understood, and do not influence crater shadow lengths. Furthermore, use of SPC models enables

[1] The official International Astronomical Union name is Charlois Regio. We choose to use Shoemaker in this study to remain consistent with previous literature.

global crater morphology measurements regardless of illumination conditions (for shadow-based measurements) or the alignment of an NLR track with a crater center.

Here, we measure eight profiles for each crater (see Methods Sec. 1) and, unlike shadow measurements, our method does not assume a crater shape. This approach allows us to obtain a more accurate measure of the depth-to-diameter ratio including natural sources of uncertainty commonly leading to profile-to-profile variations in the size and depth of the crater [Robbins et al. 2018]. This method allows us to more accurately capture the effect of regional topography, which is important for small and irregularly shaped asteroids. Fig. 1 shows the hill-shaded relief of three example craters of varying *d/D* with geometric height, the height above a regional plane [Barnouin et al. 2020], contours over-plotted (left panels) and the corresponding eight crater profiles (right panels).

We find that the global average *d/D* ratio for craters in our survey is 0.128 +/- 0.03 (Extended Data Fig. 1a). This value is small compared to an 'ideal' fresh lunar crater ratio of 0.2 [Pike, 1977]; however, it is closer to the mean *d/D* value on other asteroids (~0.15 [Marchi et al. 2015]), and close to the global mean of 0.12 found from shadow measurements of these same craters by [Robinson et al. 2002]. There is a larger spread in *d/D* values at smaller sizes, and craters 500–1000 m in diameter exhibit the largest degree of degradation (Extended Data Fig. 1b). The minimum *d/D* measured was 0.047 ± 0.015 (Crater 430, 43º S, 63ºN), though shallower craters may be difficult to identify. The maximum *d/D* measured was 0.23 ± 0.01 (Crater 017, 13ºN, 164.0ºE), higher than the 0.2 value typical of fresh lunar craters and asteroids. We use our measurements to elucidate the physical evolution of Eros' surface.

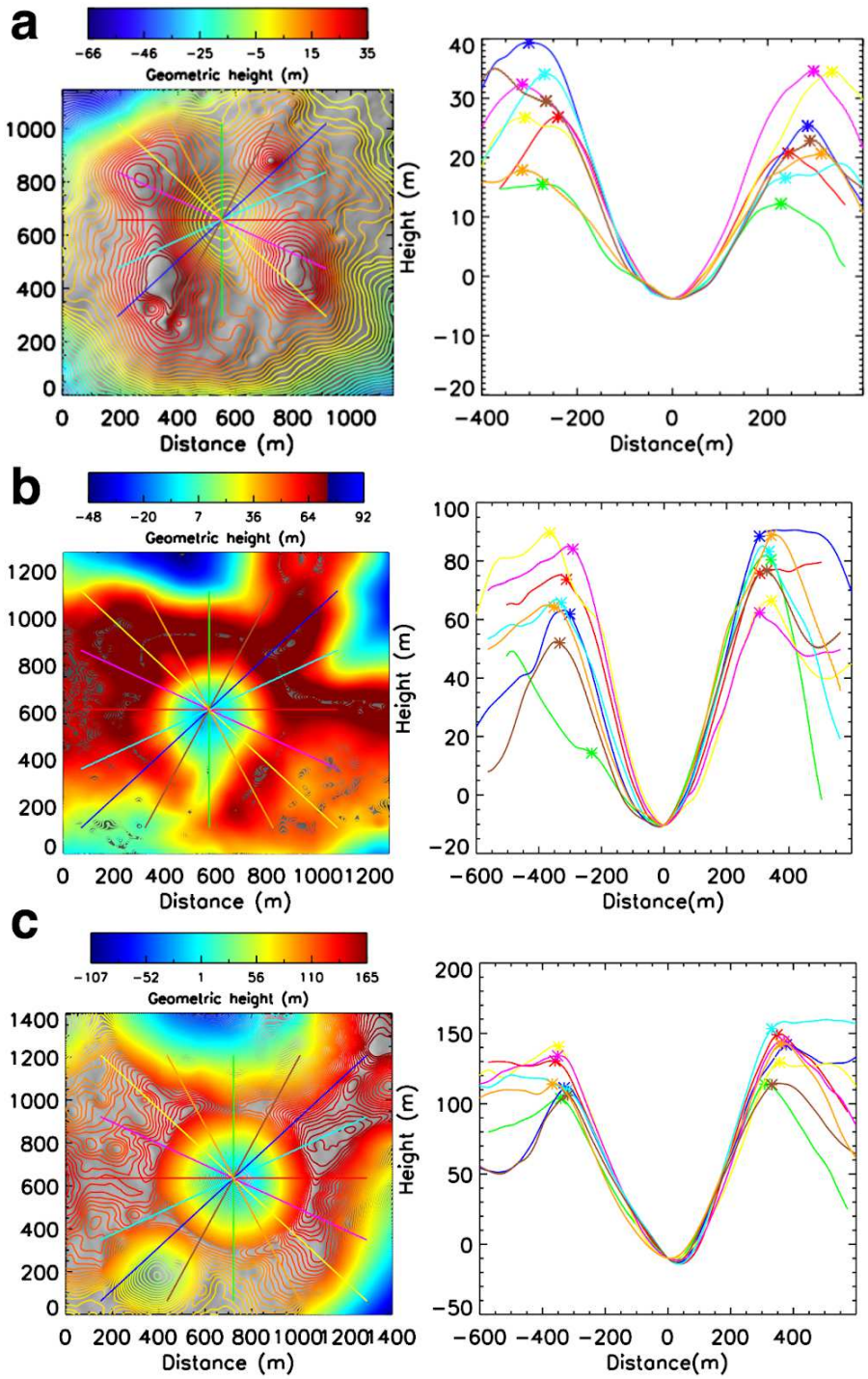

Figure 1. Examples of local DTMs of Eros craters (contour maps of geometric height in left panels) and their measured profiles (right panels). Eight profiles, with origins at the crater center and equally spaced in the azimuthal direction, are used to obtain a robust measurement of crater morphology. Each profile has two asterisks that mark the positions of the crater rim. **a,** example of a shallow crater, CRT328G (65ºS, 19ºE), d/D = 0.056 +/- 0.016. **b,** example of a crater with average d/D, CRT210G (3ºN, 310ºE), d/D = 0.130 +/- 0.011. **c,** example of a deep crater CRT095 (32ºS, 225ºE), d/D = 0.205 +/- 0.020.

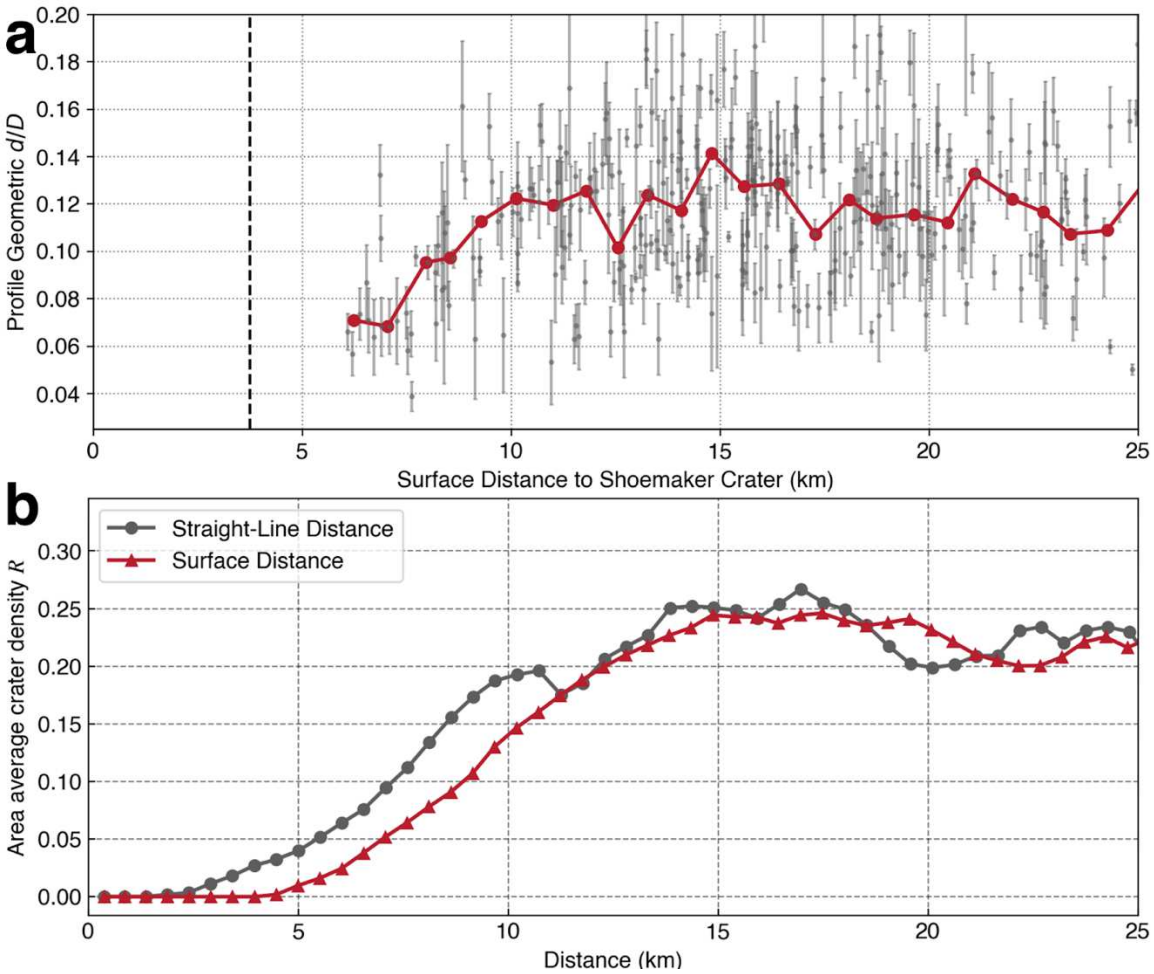

Figure 2. Evidence of crater depletion and degradation surrounding Shoemaker crater. **a**, the geometric *d/D* of craters (grey circles) increases as a function of distance from the center of Shoemaker crater for craters with $D > 500$ m, up to a distance of ~10–12 km. The red curve shows the moving average (median) of the grey circles). The vertical black dashed line marks one crater radius. **b**, the area average crater density, *R*, of craters with $D = 500$–2000 m also increases as a function of straight-line (euclidean, grey curve with circles, similar to Fig. 2b of [Thomas & Robinson 2005]) and surface (geodesic, red curve with triangles) distance from the center of Shoemaker crater.

Crater *d/D* in proximity to Shoemaker Crater

A spatial analysis of our crater morphology measurements reveals that the *d/D* of craters with $D > 500$ m increases with distance to Shoemaker crater (red curve Fig. 2a), before reaching a steady value of ~0.12 at distances of ~10 km. A similar analysis for smaller ($D < 500$ m) craters found no clear trend (Extended Data Fig. 1c). Furthermore, no other clear trend of *d/D* with distance from the other large craters on Eros ($D > 2$ km) is apparent (Extended Data Figs. 2&3). Previous studies of Eros have shown that the large boulder population (> 30 m-diameter) likely tracks ejecta from Shoemaker crater [Thomas et al. 2001], and the relative crater density is shallowest in a region surrounding the same crater [Thomas & Robinson 2005]. In Fig. 2b, we used a shape model of Eros with a mean facet length of 150-m [Gaskell et al. 2008] to reproduce the analysis of [Thomas & Robinson 2005] showing the increase in the area average crater density, *R* (the mean crater density within 2-km x 2-km bins for craters with $D = 0.5$ to 2 km) as a function of straight-line distance from the center of Shoemaker crater (grey curve with circles). We also show how crater *R* varies with surface distance from Shoemaker crater (red curve with triangles), which we define as the shortest distance along the surface to Shoemaker crater (i.e. the geodesic). We find that crater *R* reaches a value of > 0.2 at a straight-line and surface distance of approximately 10 and 12 km, respectively. The rightward shift of the red curve compared to the grey may be indicative of an erasure mechanism that depends on surface distance from Shoemaker, rather than the straight-line distance as posited by [Thomas & Robinson 2005].

The similarity in trends in the *d/D* and crater *R* with surface distance (Fig. 2) spurred us to further investigate correlations in three-dimensional space. Fig. 3 shows the variation in *d/D* (Figs. 3a–c) and crater *R* for craters with D=0.177-1 km (Figs. 3d–f) projected onto the shape model of Eros [Gaskell 2008]. The size range of craters in Figs.3d–f was chosen to directly compare to the analysis of [Thomas & Robinson 2005]. We highlight the three largest craters on Eros (Himeros, Shoemaker, and Psyche) in black (Figs. 3a,b). Using the Small Body Mapping Tool [SBMT, Ernst et al. 2018], we mapped a continuous region of shallow craters that surrounds Shoemaker (shown in magenta). We term this region the *Shallow Crater Region* of Eros, which makes up ~ 20% of Eros' surface area. Fig. 3f highlights the Shoemaker-crater antipode, where an arrow-head pattern of crater depletion is apparent, noted by [Thomas & Robinson 2005] as possible evidence for a seismic resurfacing event generated by the Shoemaker-forming impact. We note that this arrow-head pattern disappears when large craters are considered ($D = 0.5$ to 2 km, Fig. SD). Here, we do not find a similar spatial pattern emerging in the *d/D* data (compare Fig. 3b to Fig. 3e).

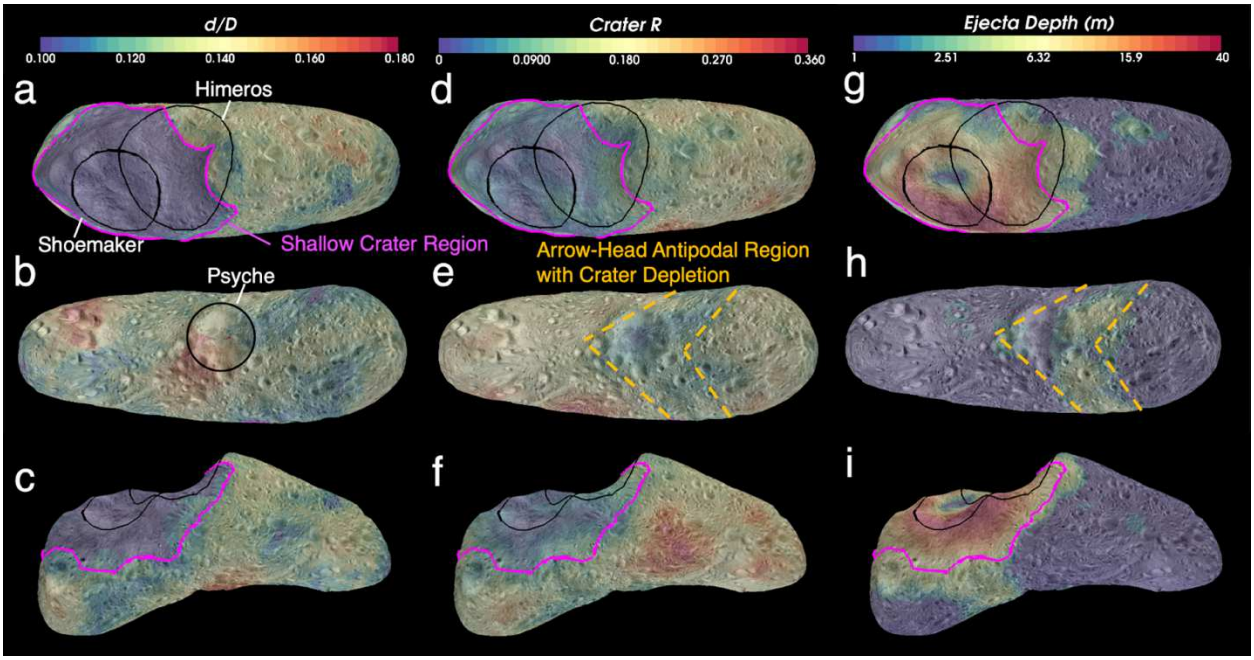

Figure 3. Crater *d/D*, crater *R*, and simulated ejecta depth projected onto an Eros shape model generated using the SBMT [Ernst et al. 2018], **shown with a projected basemap of Eros [**Stooke et al. 2015**].** Both *d/D* and crater *R* are at a minimum in a region surrounding Shoemaker crater. **a–c**, Three views of the area average *d/D* of craters on Eros, with **a** centered on (0º N, 90º E), **b** centered on (0º N, 270º E), **c** centered on the southern pole, and North is up in **a** and **b**. We mapped the *Shallow Crater Region* in magenta. **d–f,** Three views of the crater *R* of Eros' surface for craters that have D = 0.177 to 1 km (similar to Fig. 1 of [Thomas & Robinson 2005]). The antipodal region of Shoemaker crater, **e**, exhibits an arrow-head shape region with small values of crater *R*. **g-i,** Three views of the ejecta depth from numerical simulations of ejecta deposition using *pkdgrav*. The ejecta depth is largest on the southern rim of Shoemaker, but the values are not large enough to explain the observed crater degradation. However, ejecta deposition may explain the decrease in crater *R* at the antipodal region (**h**), as the simulations reproduce the arrow-head pattern.

Shoemaker Region Resurfacing and Crater Degradation: Ejecta Contributions

For small asteroids, a variety of mechanisms have been suggested for surface refreshing and crater degradation such as crater superposition, burial by impact ejecta, impact-induced seismic shaking, tidal forces, and surface destabilization through changes in spin state [Marchi et al. 2015]. On Eros, the density of craters (D < 500 m) falls well below those for equilibrium saturation [Chapman et al., 2002], ruling out crater superposition as the cause for the observed small crater deficit. Furthermore, changes to the spin-state of Eros due to the YORP effect occur in timescales that are orders of magnitude longer [Bottke et al. 2006] than its estimated dynamical lifetime in near-Earth space. Thus, the most plausible mechanisms for crater degradation on Eros are impact-induced seismic shaking [Richardson et al. 2005] and/or ejecta deposition.

The contribution of Shoemaker ejecta on crater burial was previously explored by [Thomas & Robinson 2005] who concluded that the ejecta were unlikely to be important for the following reasons: i) an analytical calculation of ejecta trajectories using a Maxwell Z-model does not match the arrow-head pattern east of Psyche (Fig. 3e), ii) the distribution of large boulders (D > 30 m), which was taken as a proxy for the distribution of low-velocity Shoemaker ejecta, does not geographically match the observed crater deficiencies, and iii) the volume of ejecta is small relative to that required to achieve complete crater in-filling. By ruling out ejecta as a mechanism for crater depletion, [Thomas & Robinson 2005] concluded that seismic shaking was the sole mechanism for crater depletion stemming from the Shoemaker-forming impact. tHere, we revisit this topic in light of our new measurements and with a better suited method for calculating the dynamical fate of ejecta launched from an irregularly shaped body.

In order to investigate the relative contribution of crater ejecta deposition on the d/D of craters surrounding Shoemaker, we performed a series of direct N-body simulations that tracked the fate of particles ejected from Shoemaker. We used the N-body collisional code *pkdgrav* [Richardson et al. 2000] combined with empirical scaling relationships for the velocity distribution of ejecta following a hypervelocity impact [Housen & Holsapple 2011] (see Methods Sec. 2). Extended Data Fig. 3 shows snapshots from one of the *pkdgrav* simulations. We allowed the ejecta to evolve for approximately 2 weeks of simulated time, tracking its landing position on Eros. The two weeks of simulated time is much longer than the crater formation timescale of Shoemaker (on the order of 10 minutes or less), and was sufficient to determine the eventual fate (escape or re-impact) of > 99% of the simulated ejected particles.

By tracking the ejecta that are deposited across Eros, we measure the total change in depth across different regions (Figs. 3g–i). We note that the maximum ejecta depth is 40 m, which would be sufficient to erase a 650 m crater, if it had an initial d/D of 0.13 (the global mean value). However, this magnitude of burial by ejecta is limited to a region that is mostly concentrated within Shoemaker crater itself and near its southern rim. For the majority of the *Shallow Crater Region*, the average ejecta depth only amounts to 6–10 m, which would only be sufficient to bury 100–180 m-diameter craters if they had an initial d/D of 0.13. The same magnitude of ejecta deposition (6–10 m) would cause relatively little degradation of a 500-m crater, such that an initial d/D = 0.13 would become $d/D \sim 0.1$.

While the volume of ejecta may not be sufficient to explain the degradation of most craters immediately surrounding Shoemaker crater, it may explain the depletion of small craters (< 500 m) at the antipode. We find that the simulations consistently produce ejecta patterns with an arrow-head shape at the antipode (Fig. 3h). This pattern emerges due to Eros' unique shape, with some contribution from its spin state (Eros is a relatively fast principal axis rotator with a spin period of 5.27 hrs). Material that is ejected in the east and west directions are immediately swept up by the rotating body. In contrast, material that is ejected in the north and south directions are able to be deposited easily onto the antipode as the ballistic distance traveled is relatively short due to the shape of the asteroid. We took into consideration that Eros may have had a different rotation state at the time of Shoemaker crater's formation by running additional simulations with Eros spinning with periods of 4 h (faster spin), 8 h (slower spin), and with no spin at all. We find that an arrow-head pattern emerges for all of these cases, with a marginal increase in ejecta depth with slower spin (up to 1.5x the values shown in Figs. 3g-i, see Extended Data Fig. 5).

The production of an arrow-head pattern suggests a non-negligible influence of ejecta for crater degradation, refuting reason (i) of [Thomas & Robinson 2005] used to support their conclusion that ejecta do not contribute to crater depletion in the antipode. Furthermore, we also refute reason (ii) of [Thomas & Robinson 2005] as the volume of mapped large boulders by [Thomas et al. 2001] only represents 1% of the total volume of re-impacting ejecta, based on our simulations. Furthermore, studies have demonstrated that larger ejecta are typically deposited closer to the crater rim than smaller ejecta [Oberbeck 1975]. Therefore, we determine that the large boulders are a poor proxy for understanding the fate of all ejecta. Concerning reason (iii) of [Thomas & Robinson 2005], we concur that the volume of ejecta is insufficient to explain burial of craters by proximal ejecta; however, we have shown that these ejecta may have been sufficient to erase the small crater population (D < 500 m) in the antipode, while keeping the large crater population (D > 500 m) relatively undegraded, which may explain the mismatch in spatial patterns of the antipode between the maps of crater R and d/D in Figs. 3b and 3e. Furthermore, work by [Minton et al. 2019] on the degradation of lunar craters has shown that, unlike the spatially uniform blanketing by proximal ejecta, distal ejecta can induce mass movement and mixing upon deposition through ballistic sedimentation [Oberbeck 1975]. The ejecta deposited at the antipode have specific impact energies ~ 4 times greater than those deposited in the center of nearby Himeros crater and ~ 11 times greater than those deposited just beyond the Shoemaker crater rim. As the surface gravity on Eros is small compared to the Moon (~5 mm/s^2 at the antipodal region), even low velocity impacts close to its escape speed (~ 5 m/s) can lead to agitation and displacement of regolith [Ballouz et al. 2021].

Shoemaker Region Resurfacing: Seismic Shaking Contributions

As ejecta deposition can plausibly explain the crater depletion pattern at the antipode, but not the crater degradation pattern surrounding Shoemaker, we explored how our crater morphology measurements may provide new constraints on impact-induced seismic shaking and the Eros interior. Thomas & Robinson [2005] argued that a seismic shaking event stemming from the Shoemaker crater impact caused regional resurfacing Eros. However, [Thomas & Robinsons 2005] presented a cursory exploration of the seismic shaking mechanism, showing a correlation between crater R and the square of straight-line distance, a presumed geometrical scaling for seismic body wave dissipation. In contrast, [Richardson et al. 2005] used numerical models of impact-induced

global seismicity to argue that crater degradation on Eros proceeds through the cumulative effect of its impact history. [Richardson et al. 2005, 2020] showed that impactors as small as 1-m may induce global seismic shaking on Eros, leading to the down-slope diffusion of material and the eventual degradation of craters.

Why then is the observable extent of seismic damage from Shoemaker crater limited to an area that is only ~ 20% of Eros' surface? To answer this question, we combined our measurements of crater *d/D* in the vicinity of Shoemaker crater with a first-principle analysis of seismic wave propagation [Aki & Richards 1979, Richardson et al. 2005] and using the mathematical descriptions for crater degradation through regolith downslope diffusion [Melosh 1989]. As we have shown that craters with $D > 500$ m within a surface distance of ~ 12 km of Shoemaker crater were likely degraded after its formation, we isolate these craters and measure the magnitude of downslope material diffusion, K, required to degrade each crater to its observed state (Methods Sec. 3). As the initial *d*/*D* of these craters is unknown, we run a Monte Carlo simulation, randomizing each crater's initial *d/D* based on the observed distribution of crater *d/D* outside the resurfacing region. The simulation provides an uncertainty estimate on the value of K for each crater. We find a clear decrease in K as a function of surface distance (Fig. 4a), and model this decay through the propagation of a seismic wave from the center of Shoemaker. We show that this model is consistent with observations and our current knowledge of the seismic properties of planetary surfaces.

We posit that the dominant contributor to seismic damage was surface waves rather than body waves, since: 1) the decrease in crater R extends to further surface distances compared to straight-line (interior) distance (Fig. 2b), 2) the *shallow crater region* is confined to an area that immediately surrounds the Shoemaker crater and does not extend to its antipode (body waves have a relatively short 10-km path to the antipode compared to > 20-km for surface waves), and 3) antipodal crater erasure can be plausibly explained by the deposition of Shoemaker crater ejecta (Figs. 3e,h). Thus, we model the attenuation of a surface wave as a function of surface distance from the impact point (center of Shoemaker crater), as tracked by the value of K for degraded craters. In Methods Sec. 4, we show that, for a Rayleigh surface wave, K decreases as an exponential function of distance, r, such that $K \propto e^{-r/\alpha}$, where $\alpha = 12\ \xi / V_R$. ξ is the seismic diffusivity of the Eros regolith, and V_R is the seismic wave speed. By fitting an exponential decay function to our estimated values of K for each crater, we find that $\alpha = 2.40$ +/- 0.61 km. For $V_R =$ 100 m/s, similar to lunar regolith [Nakamura 1976], our measurements suggest that the seismic diffusivity of Eros regolith, $\xi = 0.02$ +/- 0.005 km^2/s. This value is consistent with the seismic diffusivity estimated for lunar regolith, 0.02–0.03 km^2/s from moving robotic rovers [Nakamura 1976]. This analysis also provides a direct means to estimate the scattering length, L_S, as $\xi = V_R L_S /3$ [Toksoz et al. 1974], which described the mean free path of seismic waves as they diffuse from the source [Nakamura 1976]. We find that $L_S = 602$ +/- 154 m, which is also consistent with the scattering length of lunar regolith (on the order of 100-300 m) [Nakamura 1976, Toksoz et al. 1974] and that determined for Eros from statistical analysis of global crater erasure on Eros through the effect of its cumulative impact history (250-1000 m) [Richardson et al. 2005].

Rayleigh surface waves typically have the largest amplitudes of all seismic waves, and these attenuate more slowly than body waves [McGarr et al. 1969]. These properties of seismic waves may explain the apparent dichotomy between the regional influence of seismicity from the Shoemaker impact [Thomas & Robinson 2005], compared to the expected global seismicity of

impacts based on modeling of body waves [Richardson et al. 2005]. Surface seismic waves generated from impacts have yet to be observed on the Moon, potentially due to the presence of strong scatterers in the near surface [McGarr et al. 1969]; however, they have been observed on Mars in association with meteorological phenomena [Hobinger et al. 2021]. The general shape of the *Shallow Crater Region* is an ellipse centered on Shoemaker that extends further to the East and West than to the North and South. This shape may be explained by the presence of lineaments that encircle Shoemaker Crater and Himeros. In particular two sets of lineaments mapped by [Buczkowski et al. 2008], Lineament Set#1 and #3, border the *Shallow Crater Region* immediately to the North and South (Fig. 4b). These lineaments are oriented perpendicular to longitudinal waves moving radially outward from the center of Shoemaker. Fig. 4b shows how the Set#3 lineaments mapped by [Buczkowski et al. 2008] overlap with the Southern edge of the *Shallow Crater Region*. Spacing between lineaments in this set ranges from 200–800 m, which is similar to our measured value of L_s for surface waves. If the lineaments represent large fractures within Eros, they may have confined impact-generated seismic waves to a local region, and frustrated their propagation globally.

Our modeled decay of the K as a function of distance provides insights into the limits of seismic shaking from the Shoemaker-forming impact at contributing to global resurfacing and crater erasure on Eros. For a given value of K, the maximum crater size that could be erased by down-slope diffusion can be determined (Methods Sec. 3). Based on parameter fits shown in Fig. 4a, we show the largest crater that could be erased by seismic shaking from Shoemaker crater as a function of distance from its center (Fig. 4c). We note that a surface wave would only erase < 70-m-diameter craters in the antipodal region (a surface distance of >20 km). Globally, the surface wave could have only erased craters with D < 3.5 m. In the *Shallow Crater Region*, which extends out to a surface distance of 10–12 km, our model predicts the complete erasure (can no longer be detected due to sufficiently shallow d/D) of craters with D < 250–350 m (Methods Sec. 3).

Ejecta deposition works to increase the maximum crater size erased by the Shoemaker-forming impact. A crater with D = 500 m at a surface distance of 10 km would degrade from a mean d/D = 0.13 to 0.05. A crater with d/D = 0.05 would still be detectable in our sample. The ejecta layer of 6–10 m, determined by our ejecta simulations, would further degrade such a crater from a d/D = 0.05 to 0.02–0.01, which would make it effectively undetectable. Therefore, the combination of seismic shaking and ejecta deposition from Shoemaker impact erased craters with D < 500 m within 10 km of the Shoemaker center. These results are consistent with our observation that craters with D < 500 m exhibit no degradation pattern with distance from the center of Shoemaker crater (Extended Data Fig. 1c). We conclude that the current population of D < 500 m inside the *Shallow Crater Region* was created after the formation of Shoemaker crater.

Based on lineament mapping, [Buczkowski et al. 2008] determined that a small subset of lineaments may have been inherited from the Eros parent body. Numerical simulations show that the impact that formed Himeros (the largest crater on Eros) would have shattered the body and produced the majority of fractures within Eros [Tonge et al. 2019], possibly re-activating inherited pre-existing flaws. Subsequent cratering by impacts all smaller than Himeros probably only reactivated nearby internal flaws, with limited seismic activity and only local resurfacing through surface seismic waves and ejecta, as seen here for the Shoemaker impact. To generalize, the shattering impact on an asteroid may cause global seismic resurfacing and reset its surface age

[Asphaug 2008], creating wide-spread lineaments. However, subsequent impacts, even those generating craters that approach half the asteroid size, will only have local re-surfacing effects.

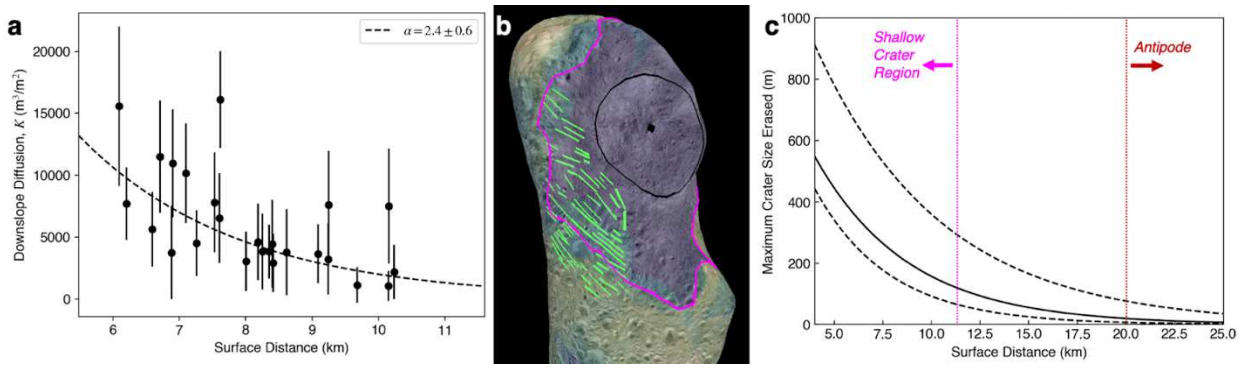

Figure 4. a, For each crater within 10 km of the center of Shoemaker crater (black dots), we measured the downslope diffusion constant, *K*, needed for the crater to evolve from an initial *d/D* drawn randomly from the distributions shown in Extended Fig. 6b to its current *d/D*. We performed a monte-carlo simulation with 50 random draws of initial *d/D* in order to obtain an uncertainty estimate for *K* (black error bars). We then found the best-fit solution to the decay of the seismic wave (dashed curve), which gives $\boldsymbol{\alpha}$ = 2.40 +/- 0.61 km, which translates to a seismic diffusivity, ξ = 0.02 +/- 0.005 km^2/s, similar to lunar regolith. **b**, Snapshot of an Eros shape model in the SBMT overlain with colors representing the regional mean *d/D* of craters (see Fig. 3 for color map). Mapped on the shape model are the *Shallow Crater Region* (magenta), lineament Set #3 from [Buczkowski et al. 2008] (green lines), and Shoemaker crater (black circle) and its center (black square). The lineaments may be expressions of near-surface fractures that scatter and focus seismic surface waves traveling from the center of the crater. **c,** The maximum crater size erased by our modeled surface seismic wave as a function of distance. The black solid line represents our nominal solution, and the dashed lines show the model's 1-sigma uncertainties. Craters with $D <$ 250–350 m with the *Shallow Crater Region* are erased by the seismic wave alone. At the antipode, only craters with $D <$ 70 m could have been erased by the seismic wave.

The Age of Shoemaker Crater

Our analysis shows that all craters with $D > 500$ m in the *Shallow Crater Region* predate Shoemaker because their degradation state indicates they were affected by the impact that formed Shoemaker. Craters with $D < 500$ m craters were erased by the Shoemaker-forming impact through a combination of seismic shaking and ejecta deposition. Therefore, we can estimate the age of Shoemaker crater by examining the population of $D < 500$ m craters within the *Shallow Crater Region*. We obtained crater counts from [P. Thomas (private comm.)] and augmented these by performing our own crater counts in the *Shallow Crater Region*. In total we measured an additional ~1000 craters with diameters between 0.06 and 1 km, for a total count of ~1,400 craters in the *Shallow Crater Region* (Fig. 5a). We analyzed the cumulative size frequency distribution (CSFD) of these craters and determined that our counts are complete down to a $D = 120$ m. For craters with $D = 120$–500 m, the CSFD follows a power law with an exponent of -2.51 +/- 0.01, which is similar to the crater production function of main belt asteroids [Bottke et al. 2020]. This regional count allowed us to obtain a robust measurement of the cratering history on Eros after the Shoemaker impact.

As Eros is a NEA, we considered two possible populations of impactors: i) main belt asteroids (MBAs), and ii) near-Earth objects (NEOs) (Methods Sec. 5). While the number of potential impactors in the main asteroid belt is higher than in near-Earth space, the encounter speeds in the main belt are generally lower by a factor of approximately 4. For MBA impacts, the impact flux model of [Bottke et al. 2005] is used. For NEO impacts, the impactor flux model of [Brown et al. 2002] is used, scaling for target size and neglecting gravitational focusing. The primary factor driving the uncertainty in the crater production function is the strength of the Eros surface. We consider two end-member cases: a gravity-dominated case, as informed by cratering experiments on small bodies [Schultz et al. 2007, Arakawa et al. 2020], and a strength-dominated case as informed by collisional balance in the main asteroid belt [Bottke et al. 2020]. In Fig. 5b, we show that the production of craters in the *Shallow Crater Region* is modeled well by a main belt production curve, giving an exposure age of 6.5±1.6 Myr for gravity-controlled cratering, and 31.8±6.7 Myr for strength-controlled cratering. For NEO impacts, an exposure age of 130 and 600 Myr is required for gravity- and strength- controlled cratering, respectively. Therefore, the production of craters with $D = 120$ - 500 m in the *Shallow Crater Region* is unlikely to have happened in near-Earth space as NEAs have dynamical lifetimes of only 10–100 Myr [Bottke et al. 2001]. Therefore, we conclude the majority of these craters formed when Eros was still dynamically coupled to the main asteroid belt.

The young surface age for Shoemaker has important implications for our understanding of NEAs collisional and dynamical evolution. Due to their short lifetimes, NEAs must originate from a larger reservoir of asteroids, the main asteroid belt [Bottke et al. 2001], where the catastrophic disruption of large-scale (100-km sized) asteroid parent bodies [Zappala et al. 1995] creates families of new asteroids. However, recent spacecraft observations of small km-scale rubble-pile NEAs and analyses of samples returned from their surfaces show that their surface ages are 10 to 100 times younger than their candidate asteroid family ages [Walsh et al. 2019, Sugita et al. 2019, Arakawa et al. 2020]. Proposed resolutions to this inconsistency have been that km-scale NEAs are the end-product of a cascade of catastrophic disruptions initiated by that of their main belt parent body [Sugita et al. 2019, Walsh et al. 2020], or, alternatively, NEAs experience substantial

resurfacing during their lifetime [Nagao et al. 2011, Binzel et al. 2010, Walsh et al. 2008, Richardson et al. 2020].

As Eros is one of the largest NEAs, its Yarkovsky drift rate as a main belt asteroid is quite slow, $< 10^{-5}$ AU/Myr [Bottke et al. 2006]. The combination of this slow drift and the young formation age of Shoemaker suggests that the Shoemaker-forming impact likely occurred while Eros was already in a main belt resonance zone [Bottke et al. 2020] that would excite its orbit into near-Earth space. If so, the Shoemaker impact event generated ejecta in a resonance zone that could directly inject those new asteroids into near-Earth space. This material may be part of a near-Earth space S-type asteroid cratering family that originated from Eros. Asteroid cratering families have been previously studied, such as Vestoids and HED meteorites originating from the 500-km asteroid (4) Vesta's Rheasilvia basin [Buratti et al. 2013]. Smaller cratering families have also been reported in the main asteroid belt, such as the asteroids dynamically associated with the 8-km-diameter (1270) Datura comprising 4.5% of the parent body mass [Vokrouhlický et al. 2017]. Here, the ejecta that are associated with the Shoemaker crater family would comprise only ~0.4% of Eros' total mass. Nevertheless, the total volume of escaping material (see Extended Data Table 1), would be equivalent to that generated from the catastrophic disruption of a 5 km-diameter asteroid. In the main belt, cratering events like the Shoemaker-forming impact occur at roughly the same rate as that of the disruption of 5-km main belt asteroids (Methods Sec. 5). Therefore, we propose that NEAs and meteorites sourced from cratering events should be as prevalent as those sourced from catastrophic disruption events.

Unlike main belt asteroid families, members of a cratering family generated in a resonance zone would be difficult to dynamically link together due to the chaotic nature of their ejection from the main belt. Nevertheless, our hypothesis may be tested by considering the cosmic ray exposure (CRE) ages of Eros' closest meteoritic analogs, H and/or LL chondrites [McCoy et al. 2001]. The 4π CRE ages of ordinary chondrites (OCs) span a wide range (0.5-80 Myr); however, the ages have peaks at 6-10 Myr for H chondrites and 15 Myr for LL chondrites [Connolly et al. 2015]. Our determined age range for Shoemaker crater (6.5-31.8 Myr) brackets these peaks in H and LL chondrite CRE ages, suggesting the possibility that a large fraction of these OCs in our meteorite collection originate from the Shoemaker-forming impact or a similar impact on a similarly sized asteroid parent body. In addition to the production of meteorite-sized objects, these cratering impacts could also produce sub-km rubble-piles through the gravitational reaccumulation of material. If so, S-type NEAs should exhibit relatively young exposure ages. Considering the example of the 300-m–diameter NEA (25143) Itokawa, recent analysis of Itokawa's surface age from crater counting, 10–33 Myr [Tatsumi & Sugita 2018], overlaps the Shoemaker-formation age. The Shoemaker age is also consistent with that derived from analysis of the cosmic ray exposure (CRE) age of Itokawa samples (< 8 Myr) [Nagao et al. 2011]. Due to the limited volume of ejecta produced by the Shoemaker-forming impact compared to the total number of S-types in the NEA population, the probability that Itokawa is a direct product of the Shoemaker-forming impact is likely low. Rather, the concurrences in ages described here suggest that the source of small NEAs and meteorites may be Shoemaker-like cratering impacts on to 10-km scale asteroids near resonance zones. Thus, 10-km scale asteroids may act as relay points in the delivery of material from the 100-km scale main belt parent bodies in dynamical stable regions to resonant escape hatches. The work here is direct evidence of the importance of large cratering events in the production of NEAs and meteorites. Furthermore, the young surface crater ages of km-scale NEAs

observed by spacecraft [Walsh et al. 2019, Sugita et al. 2019, Arakawa et al. 2020] is a consequence of a collisional cascade process augmented by cratering events, like the Shoemaker-forming impact, that produce asteroid cratering families.

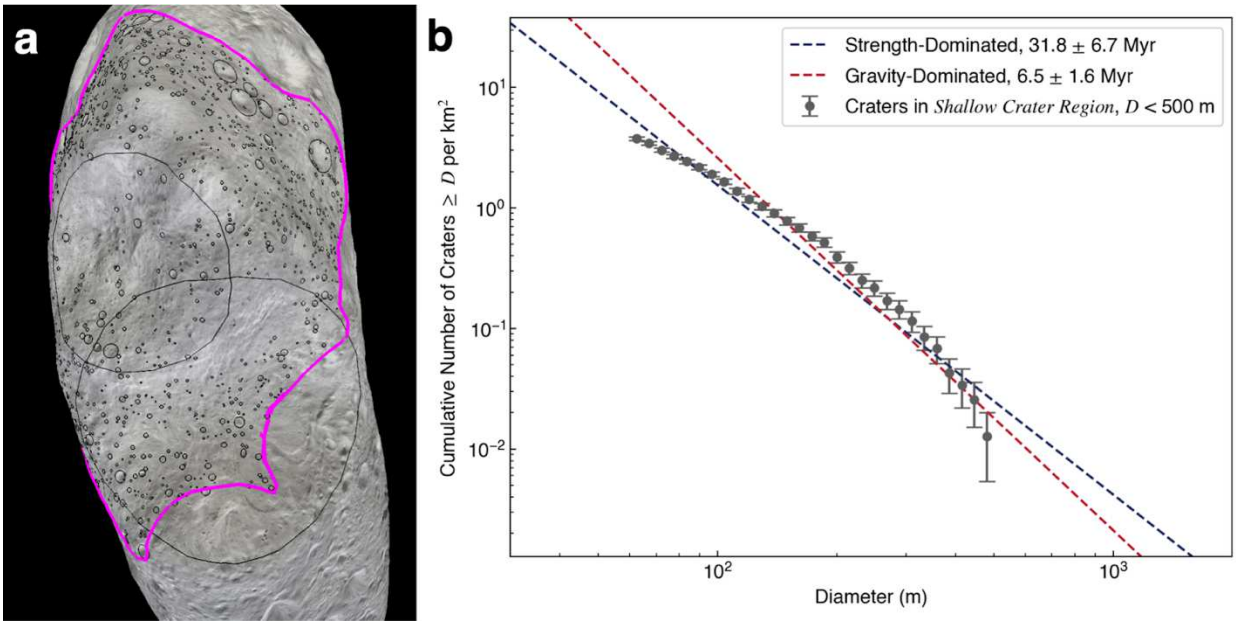

Figure 5. a, Snapshot of crater counts in the *Shallow Crater Region* (magenta). The two larger outlined craters are Shoemaker (top) and Himeros (bottom). **b**, Crater counts (grey dots with error bars) in the *Shallow Crater Region* indicate a main-belt surface exposure age of 6.5 +/- 1.6 Myr (gravity-dominated crater scaling, red dashed line) to 31.8+/- 6.7 Myr (strength-dominated crater scaling) for Shoemaker crater.

References:

1. Chapman, C. R., et al., Icarus, Volume 140, 28 (1996).
2. Bottke, W.F., et al., The Astronomical Journal 160, 14 (2020).
3. Hurford, T. A. et al. J. Geophys. Res. Planets 121, 1054–1065 (2016).
4. Binzel, R., et al. Nature, Volume 463, Issue 7279, pp. 331-334 (2010).
5. Walsh, K.J., et al. Nature, Volume 454, Issue 7201, pp. 188-191 (2008).
6. Asphaug, E. Nature Communications, Volume 11, article id. 1564 (2020).
7. Prockter, L., et al. Icarus, Volume 155, Issue 1, p. 75-93 (2002).
8. Buczkowski, D.L., et al. Icarus, Volume 193, Issue 1, p. 39-52. 2008
9. Veverka, J., et al. Icarus, Volume 107, Issue 1, p. 2-17. (1994)
10. Barucci, M.A., Asteroids IV, Patrick Michel, Francesca E. DeMeo, and William F. Bottke (eds.), University of Arizona Press, Tucson, p.433-450 (2015).
11. Richardson, J. E., et al. Icarus, Volume 179, Issue 2, p. 325-349 (2005).
12. Thomas, P.C., \& Robinson, M.S., Nature 436, 366 (2005).
13. Chapman, C.R., et al. Icarus, Volume 155, Issue 1, p. 104-118 (2002).
14. Robinson, M.S., et al. Meteoritics & Planetary Science, vol. 37, no. 12, pp. 1651-1684 (2002)
15. Thomas, P.C., et al. Nature 413, 394 (2001).
16. Hirata, N. et al. Icarus, Volume 200, Issue 2, p. 486-502. (2009)
17. Sugita, S. et al. Science, Volume 364, Issue 6437, id. eaaw0422 (2019).
18. Walsh, K.J., et al. Nature Geoscience, Volume 12, Issue 4, p.242-246 (2019)
19. Bierhaus, E.B., et al. Nature Geoscience, Volume 15, Issue 6, p.440-446 (2022).
20. Tatsumi, E. and Sugita, S. Icarus, Volume 300, p. 227-248 (2018)
21. Barnouin, O.S., et al. Icarus, Volume 325, p. 67-83. (2019)

22. Richardson, J.E., et al. Icarus, Volume 347, article id. 113811 (2020).

23. Asphaug, E. Meteoritics & Planetary Science, vol. 43, Issue 6, p.1075-1084 (2008)

24. Gaskell, R.W., Gaskell Eros Shape Model V1.0. NEAR-A-MSI-5-EROSSHAPE-V1.0. NASA

25. Planetary Data System. (2008a).

26. Marchi S., et al. Cratering on asteroids. In Asteroids IV (P. Michel et al., eds.), pp. 725–744. Univ. of Arizona, Tucson. (2015).

27. Robbins, S.J., et al. Meteoritics & Planetary Science 53, 583–637 (2018).

28. Pike R. J. (1977) Apparent depth/apparent diameter relation for lunar craters. Proc. Lunar Sci. Conf. 8th, pp. 3427–3436.

29. Ernst, C.M., et al. LPSC 49, 1043 (2018).

30. Stooke. P., Stooke Small Bodies Maps V3.0. MULTI-SA-MULTI-6-STOOKEMAPS-V3.0. NASA Planetary Data System, (2015)

31. Bottke, W.F., et al. Annual Review of Earth and Planetary Sciences, vol. 34, 157-191(2006).

32. Richardson, D.C. et al. Icarus 143, 45 (2000).

33. Housen, K. R., \& Holsapple, K. A., Icarus 211, 856 (2011).

34. Minton, D.A., et al. Icarus, Volume 326, p. 63-87 (2019).

35. Oberbeck, V.R., et al. Reviews of Geophysics and Space Physics, vol. 13, May 1975, p. 337-362.

36. Ballouz, R.-L., et al. Monthly Notices of the Royal Astronomical Society, Volume 507, Issue 4, November 2021, Pages 5087–5105 (2021).

37. Aki, K., & Richards, P. G. (1969). Quantitative seismology (2nd ed.). Herndon: University Science Books.

38. Nakamura, Y. Bulletin of the Seismological Society of America, 66(2), 593–606. (1976).

39. Toksöz, M. N., et al. Reviews of Geophysics, 12(4), 539–567. (1974).

40. McGarr, A., et al. Journal of Geophysical Research, 74(25), 5981–5994. (1969).

41. Hobinger, M., et al. Nature Communications, Volume 12, article id. 6756 (2021).

42. Tonge, A.L., et al. Icarus, Volume 266, p. 76-87. (2016)

43. Bottke, W.F., et al. Icarus 19, 63-94 (2005).

44. Brown, P. et al. Nature 420:294-296 (2002).

45. Schultz, P.H., et al. The Deep Impact oblique impact cratering experiment (2007).

46. Arakawa, M., et al. Science, Volume 368, Issue 6486, pp. 67-71 (2020).

47. Bottke, W.F., et al. Science, Volume 294, Issue 5547, pp. 1693-1696 (2001).

48. Zappalà, V., et al. Icarus, Volume 116, Issue 2, p. 291-314 (1995)

49. Nagao, N., et al. Science, Volume 333, Issue 6046, pp. 1128- (2011).

50. Vokrouhlický, D. et al. Astronomy & Astrophysics, Volume 598, id.A91, 19 pp. (2017)

51. Fujiwara, A., et al. Science 312, 1330 (2006).

52. McCoy, T. et al. Meteoritics & Planetary Science, vol. 36, no. 12, pp. 1661-1672 (2001).

53. Conolly, H.C., et al. Earth, Planets and Space, Volume 67, article id.12, 6 pp.(2015)

Methods

1. Crater Shape Models

1.1 Crater Shape Models: Stereophotoclinometry (SPC)

SPC is a well-established method of constructing shape models using images, and it has been used to generate both global DTMs of planetary objects [Gaskell et al. 2008] as well as local DTMs of geologic features of interest [Daly et al. 2020]. The detailed workings of SPC are described in [Gaskell et al. 2008]. Here, we provide a brief description. To begin, a patch of surface, or maplet, surrounding a chosen landmark is modeled digitally to match images with a range of resolutions, incidence angles, and emission angles. Cross-correlation of the imaging data with several views of the modeled maplet pinpoints the location of the landmark. Once many landmarks have been located in many images across a body, a linear minimization of the sum-squared residuals between the observed and modeled landmarks yields a solution for each landmark's position on the body, the spacecraft attitude, and the location and rotation of the body. Additional information is employed to improve this solution, such as the position of landmark maplets on the limbs of some images, correlations of adjacent maplets due to common topography, and nominal spacecraft trajectory information.

The topographic modeling of each maplet takes advantage of 2D photoclinometry and stereo effects. Observed brightness variations of a patch of surface are caused by albedo variations and the orientation of each surface element with respect to the sun and the camera. These variations constrain the slope and albedo at each maplet pixel using a linear minimization of the summed-square brightness residuals between the maplet and many images with different viewing geometries and illuminations. A Monte Carlo integration allows the determination of local terrain heights relative to the landmarks. Height constraints from overlapping or lower-resolution maplets, limbs, and geometric stereo are critical for deriving the normalized photometric function for image radiometry that relates slope to albedo, as no *a priori* function is assumed. The resulting normalized photometric function provides the basis for extrapolating the stereo-derived topography in low-resolution maplets to the high-resolution SPC topography.

The use of the SPC shape model allows the measurement of any profile across any crater on the surface of Eros, not limiting the dataset to those craters with NLR tracks through their centers. The highest-resolution global SPC shape model consists of 1.57 million vectors and was constructed from MSI images [Gaskell et al., 2008]; higher-resolution maplets which were used to derive the global shape model, were used in this study to construct local DTMs (3-m ground sample distance) to measure crater diameter, depth, and local slope, in order to get the highest possible resolution for the measurements. Extended Data Fig. 7 shows a comparison between an MSI image and a SPC shape model maplet of the 2.2 km-diameter crater Eurydice, depicting the quality of the SPC data.

The properties of the craters were measured by:

1. Mapping out the location of the crater rim using a rendered image of the topography and the high-resolution contours as a guide.
2. Fitting an ellipse to the crater rim and using the mean of the ellipse dimensions to estimate a diameter and compute an estimate of the standard deviation.
3. Fitting a plane to the mapped rim, and using this plane and the diameter, computed in step 2, to measure the crater depth from the height above the plane.
4. Estimating the uncertainty by using two rim fits: one for the 90% best fit rims height, and one for the entire rim heights, giving a more representative error.
5. Displaying contours on a DTM visualization and hand-picking the depth as the reasonable lowest point in the crater. This step was done by hand as numerical procedures may sometimes select a smaller crater within the crater being measured.

We also measured crater dimensions through the use of crater profiles by:

6. Constructing eight profiles across the hand-picked crater center.
7. Verifying the automatically detected crater rims by comparing their locations on the rendered image and to other profiles.
8. Selecting several representative profiles by hand to compute a profile-based diameter. This step was necessary to avoid the inclusion of profiles that were difficult to measure due to influence from the local topography (e.g., superposed craters, boulders).
9. Determining depths for each profile using the same procedure as step 5.

We also measured the local slope at the site of each measured crater. To calculate the slope, first we computed the gravity field for each plate of the global SPC shape model using the methods described by [Barnouin et al. 2020] and assuming a uniform density of 2.67 g/cm^3 [Yeomans et al. 2000] across the asteroid. A uniform density assumption is reasonable, as the close match between center of figure and center of mass of Eros indicates only modest internal density or porosity variations [Yeomans et al. 2000]. Slope was then calculated for each plate as the dot product between the gravity vector and the surface normal. The slope assigned to each crater was obtained by taking the average slope values for all plates outside the crater within one crater radius of the rim in order to approximate the local slope prior to crater formation. The error for each slope measurement was taken to be the standard deviation of the averaged slope values.

1.2 Crater Shape Models: NEAR Laser Rangefinder (NLR) verification

As the use of the SPC shape modeling is critical to this study, its verification is essential. Current estimates of the NLR footprint location can be off by as much as 100 m; to reduce this uncertainty, it was necessary to combine NLR data with MSI images to ensure their pointing accuracy. High-resolution NLR gridded products, which are generated by binning together elevation along these NLR tracks, possess artificial highs or lows resulting from interpolated data and mismatches between tracks. Such uncertainties significantly influence the accuracy of any measurement attempts using the NLR gridded products, especially for small surface features. A 100-m uncertainty in the location of tracks could yield measurement errors in excess of 10% for features less than a few km across. Use of co-registered NLR and MSI data only allows topographic measurements over small arcs when the center of the MSI image covers the crater center, which severely limits the measurements that can be taken.

A sub-set of five craters were chosen to assess the accuracy of the SPC DTMs. For each of these five craters, we found all NLR tracks over a central portion of the crater DTM (built at 3-m ground sample distance, Extended Data Fig. 8). Each NLR track was adjusted to better match the DTM, and bad matches were removed. We then analyzed the residuals between the remaining NLR tracks and DTMs, and also built a DTM using those NLR tracks. The RMS differences for the five craters ranged from 1.6–2.3 m, with a mean of 1.9 m (Extended Data Table 2). The mean uncertainty in the depth of craters from measurements using SPC DTMs is ~10 m, approximately 5x greater NLR-SPC differences. The overall agreement between the NLR and SPC products validates the accuracy of the SPC shape model used in this study.

2. pkdgrav simulations of the fate of Shoemaker ejecta

We simulated the fate of ejecta from the Shoemaker-forming impact by combining ejecta scaling laws [Housen & Holsapple 2011] with direct *N*-body simulations of the gravitational and collisional dynamics of that ejecta using the code pkdgrav. *pkdgrav* is a highly parallelized *N*-body code capable of accurately simulating the gravitational and collisional interactions of *N* particles [Richardson et al. 2000].

We took the following steps to setup the simulations:

1. We created a representation of Eros in *pkdgrav* by using a low-resolution shape model [Gaskell et al. 2008] and ensuring that its mass, volume, and density matched that of NEAR observations. The result is a rigid aggregate made out of ~20,000 spheres of equal mass.
2. We used a low-resolution 3D shape model of Eros [Gaskell et al. 2008] and created an alpha shape of Shoemaker crater (see [Ballouz et al. 2019] for alpha shape details) by selecting points on the crater rim.
3. The alpha shape is used to create a pre-Shoemaker-impact surface on Eros constructed out of *pkdgrav* particles, $N \sim 10{,}000$ spheres.
4. The Shoemaker particles are given ejection velocities based on ejecta scaling laws of [Housen & Holsapple 2011].

The ejection velocities of each *pkdgrav* particle, v_{ej}, at a distance, r, from the point of impact is calculated based on the following formulation [Housen & Holsapple 2011]:

$$\frac{v_{ej}(r)}{U} = C\left(\frac{r}{a}\right)^{-1/\mu_e}\left(1-\frac{r}{n_2 R}\right)^{p}, n_1 a \le r \le n_2 R, \quad (1)$$

where U is the impact speed, R is the crater radius, μ_e is a scaling parameter related to material properties, and the constants n1, n2 and p are determined by fits to ejection velocity data. The value of R = 3.25 km, and U = 5.2 km/s, based on the average main belt impact speed. $n_1 = 1.2$, and the value of C = 0.55, μ = 0.41, n2= 1.3, and p = 0.3 are taken based on experimental results of impacts on to sand targets with 35% porosity. Additional simulations where μ_e = 0.35 and 0.55 were performed to evaluate sensitivity of outcomes with μ_e.

5. With ejection velocities for Shoemaker defined, the spin properties of the entire asteroid, including Shoemaker particles, are modified. Here, we varied the spin period (4h, 5.27h, 8h, and no spin) in order to evaluate its influence on ejecta deposition.
6. The simulation is then allowed to run for two weeks of simulated time, which is much longer than expected crater formation timescale for Shoemaker (~10 minutes). More than 99% of the ejecta that are bound to Eros are reaccumulated at the end of each simulation.
7. Here, we are chiefly concerned with the gravitational dynamics of ejected particles around an irregularly shaped body and only track the re-impact locations of each particle on the Eros body. *pkdgrav* particles may bounce or roll after impact, but, as the simulated particles are large (~50 m-diameter), we ignore this subsequent motion.
8. As the re-impact location of each particle is recorded, we can estimate the total depth of ejecta, d_{ej}, deposited at different locations on Eros by dividing the total volume of ejecta that impacts each facet of the shape model to that facet's surface area.
9. Crater degradation by ejecta emplacement is calculated by subtracting the ejecta volume deposited on to a crater with diameter, D, as $V_{cr,ej} = d_{ej}\,(\pi D^2/4)$, from the initial volume of that crater, V_{ini}, and then calculating the height of a paraboloid crater with volume V_{ini}-$V_{cr,ej}$.

3. Crater Degradation Model

We model the degradation of craters by first considering axially symmetric crater profiles. Following [Melosh 1989], the initial depth, z_i, of an axially symmetric crater as a function of radial distance, r, from the crater center can be analytically represented by the following equation:

$$z_i(r) = \frac{dD^4}{128}\int_0^\infty k^3\, exp(-k^2D^2/16)\, J_0(kr)\, dk, \qquad (2)$$

where d is crater depth, D is crater diameter, J_0 is the zeroth-order Bessel function, and k is the wavenumber. Any axially symmetric crater profile can be represented as an integral over a series of J_0 Bessel functions similar to how linear functions can be represented as a Fourier integral over sine and cosine functions.

We consider degradation of a crater due to impact-induced seismic shaking to proceed through the downslope diffusion of regolith [Richardson et al. 2005]. A general solution for the change in crater depth, z_f, as a function of radial distance is given by [Richardson et al. 2005] based on techniques outlined in [Kreyszig 1993]:

$$z_f(r) = \frac{dD^4}{128}\int_0^\infty k^3 \exp(-k^2D^2/16)\, J_0(kr) \exp(-Khk^2)dk, \qquad (3)$$

which is similar to Eq. (2) except for the additional exponential term inside the integral, $R = \exp(-Khk^2)$. This additional term, R, describes the influence of downslope diffusion events on the volume and morphology of the crater. K is the amount of downslope diffusion resulting from the

impact which quantifies the volume of material that is mobilized per unit area (m^3 m^{-2}), and h is the mobilized regolith thickness. For a constant impact energy (or seismic energy), a crater can be more easily erased for larger values of h (i.e., thicker mobilized regolith layers). Similarly, the value of K depends on the energy of the impact such that more energetic impacts lead to stronger seismic shaking and more downslope diffusion of material. A demonstration of the use of these functional forms to model crater d/D is shown in Extended Data Fig. 6a.

A crater can be considered *erased* if it can no longer be detected due to a sufficiently shallow profile. From our survey of crater d/D, we find that this occurs when $d/D < 0.02$. This limit can be combined with the definition of R to obtain an estimate for the K required to erase a crater of a given diameter, D, by setting $k = k_0 = 4/D$, the peak amplitude of the spatial waves. This gives a critical downslope diffusion value, K_c:

$$K_c \geq \frac{1.3D^2}{16h} \tag{4}$$

Which can be re-arranged to estimate the max crater size erased by a seismic wave that agitates the surface to a specifc value of K:

$$D_{max} = (16hK/1.3)^{1/2} \tag{5}$$

We model the decay of the seismic wave by numerically solving for the value of K for each crater within the resurfaced region. In this manner, we can estimate how the value of K varies as a function of distance from the center of the impact. We assume a value of h = 1 m [Richardson et al. 2005], though this value for h only serves to scale the absolute value of K, and has no bearing on our estimates of the seismic properties of Eros. For each crater we perform the following Monte Carlo simulation:

1. Randomly assign the crater an initial d/D value based on the normal distribution of d/D values of craters of its size (see Extended Data Fig. 6b).
2. Numerically integrate Eq. (3) using the randomly drawn value of d/D as an input, and using an initial guess at the value of K based on Eq. (4).
3. Perform a gradient descent with updated values of K minimizing the difference, ε, between $z_f(0)$ and the measured depth of the crater.
4. Once ε is less than some small tolerance value ($< 10^{-4}$), save the value of K that produces $z_f(0) \sim d$.
5. Repeat steps 1–4 49 more times in order to obtain an estimate on how the unknown initial d/D value of the crater influences the calculated K for the crater.
6. Repeat steps 1–5, for each crater in our sample.

4. Seismic Wave Decay Model

For impact-induced seismicity, we can define the following relationship between the impact energy, E_{imp}, and the total seismic energy, E_S:

$$E_S = \eta E_{\text{imp}}, \tag{6}$$

where η is the seismic efficiency, which describes the total amount of kinetic energy that is converted to seismic energy upon impact. Based on lunar seismology, η has been estimated to range between 10^{-6} – 10^{-4}. It has yet to be directly measured for an asteroid, though it has been estimated for the 1-km rubble pile Ryugu to be < 10^{-6}[Nishiyama et al. 2020].

Here, we are concerned with attenuation of the surface seismic wave energy as it propagates to a distance, r, due to intrinsic absorption and scattering characteristics of the surface. For a Rayleigh wave, the attenuation factor, A_t, can be written as [Aki & Richards 1969, Nishiyama et al. 2020]:

$$A_t = \exp\left(\frac{-2\pi f r}{{}^{E}Q V_R}\right), \tag{7}$$

where f is the seismic wave frequency, V_R is the Rayleigh wave speed, ${}^{E}Q$ is the effective seismic quality factor, which depends on an intrinsic absorption quality factor, ${}^{I}Q$, and a scattering loss quality factor, ${}^{Sc}Q$.

$$\frac{1}{{}^{E}Q} = \frac{1}{{}^{I}Q} + \frac{1}{{}^{Sc}Q} \tag{8}$$

In this manner, the total seismic energy decays as, $E_S(r) = \eta E_{\text{imp}} A_t$. The scattering loss quality factor, ${}^{Sc}Q$ depends on frequency and seismic diffusivity, ξ [Sato et al. 2012]:

$${}^{Sc}Q = \frac{6\,\pi\, f\, \xi}{V_R^2} \tag{9}$$

Values of ${}^{I}Q$ for the lunar surface range from ~ 2000-5000 [Dainty et al. 1974, Nakamura 1976]. ${}^{Sc}Q$ has not been measured independently of ${}^{E}Q$, but an ${}^{E}Q$ = 5 has been measured for unconsolidated sand [Daubar et al. 2018]. Therefore, In the limit where ${}^{I}Q >> {}^{Sc}Q$, Eq. (8) shows that ${}^{Sc}Q = {}^{E}Q$. In this manner, we can combine Eq. (7) and (9) to show that:

$$E_S(r) = \eta E_{\text{imp}} \exp\left(\frac{-r V_R}{3\xi}\right), \tag{10}$$

Finally, in order to compare our measured values of crater degradation to the seismic attenuation properties of the Eros surface, we consider the results of [Richardson et al. 2020], who performed a series of numerical simulations to understand the relationship between K and the properties of the impactor and target, finding the following prescription for K:

$$K \propto v_{\text{imp}}^{1/2} = \left(E_{\text{imp}}\right)^{1/4}, \tag{11}$$

where v_{imp} is the impact speed. Combining Eq. (10) and (11), the attenuating properties of the Eros surface can be constrained from estimated values of K, as:

$$K(r) = K_0 \exp\left(\frac{-r}{\alpha}\right) \quad (12)$$

where $\alpha = 12\ \xi / V_R$, and K_0 is the value of K at $r = 0$, which captures the efficiency in transfer of kinetic impact energy to seismic energy. This solution provides a further constraint on the scattering length as [Dainty et al. 1974, Toksoz et al. 1974]:

$$\xi = V_R L_s / 3 \quad (13)$$

Our observations of crater degradation allow us to estimate the value of K for craters as a function of distance, r, from the impact point, with the median values of K from our Monte Carlo simulation (Methods Sec. 3), and the standard deviation of K for each crater as our uncertainty. Using a non-linear least-squares regression technique [Virtanen et al. 2020] we fit our data to a function of the form shown in Eq. (12), which returns estimates for the value of K_0 and α. These values can then be subsequently used to estimate the maximum crater size erased as a function of distance, using Eq. (5).

5. Crater Scaling Relationships

[Holsapple & Schmidt 1987] introduced generalized formulations of crater properties based on the Buckingham π theorem, which uses dimensionless numbers to estimate the crater volume, V_C, given impactor and target properties such as impactor the impactor radius, a, impactor velocity, U, impactor mass density, δ, target density, ρ, target strength, Y, and surface gravity, g. The π group parameters are related by

$$\pi_V = K_1\left[\pi_2 \pi_4^{-1/3} + (K_2 \pi_3)^{(2+\mu)/2}\right]^{-3\mu/(2+\mu)} \quad (14)$$

and

$$\pi_V = \frac{\rho V_C}{m_i} = \frac{\rho (R_C / K_r)^3}{m_i} \quad (15)$$

where m_i is the projectile mass, and R_c is the crater radius. K_1, K_2, K_r, and μ are crater scaling constants that depend on the target material. K_r relates the radius of the crater to its volume. The π-group parameters that control the cratering efficiency, π_V, are

$$\pi_2 = \frac{ga}{U^2} \quad (16)$$

$$\pi_3 = \frac{Y}{\rho U^2} \quad (17)$$

$$\pi_4 = \frac{\rho}{\delta} \quad (18)$$

Here, we are interested in the possible cratering efficiency of the upper ~100-m of the Eros surface, as we are concerned about craters with R_c < 250 m and the maximum depth-to-diameter ratio, *d/D,* observed is ~ 0.2. Due to the low gravity of Eros and its unknown surface strength, cratering efficiency may be dominated by either the gravity term (first term inside the bracket of Eq. 14), or the strength term (second term inside the bracket of Eq. 14). We consider the end-member cases where either of these terms become dominant in order to bracket the possible cratering efficiency on Eros.

Based on our observation of *d/D*~0.2 for the largest craters on Eros, we set K_r = 1.2, and generally K_2 = 1. We assume δ = 3 g/cm^3, ρ = 2.7 g/cm^3, and g = 5 mm/s^2. For the gravity-dominated case, we consider the results stemming from the small-carry on impact experiment (SCI) on 1-km rubble pile Ryugu, part of the Hayabsua2 mission, which determined that K_1 ~ 0.15, and μ=0.41 [Arakawa et al. 2020]. Note that their in-text formulation of the π-scaling laws neglects K_r, leading to a different quoted value of K_1. For the strength-dominated case, we consider the material properties of dry soil [Holsapple & Housen 2007] which has Y=0.18 MPa, K_1 = 0.24, and μ=0.41.

6. Formation Age of Shoemaker Crater and Production Rate of Cratering Families

The formation age of Shoemaker Crater was estimated by determining the surface exposure age of the *Shallow Crater Region* to impactors that generated craters up to 500 m in diameter, *D*. In total, we mapped and measured the sizes of 1,418 craters with *D* = 16–500 m in MSI images projected onto the Eros shape model, using the Small Body Mapping Tool.

We fit a power-law curve to the CSFD of the crater diameters that has a functional form of $N(>D) = A_0 D^{\beta}$, where *N* is the cumulative number of craters greater than *D* normalized by the total collecting area, and A_0 and β are the fitting parameters. We find that the best fit has β = -2.51 +/- 0.01 for a completeness limit *C* = 120 m. The value of β is similar to the CSFD power-law exponent of the observed main belt asteroid population [Bottke et al. 2005].

We then converted our crater diameters to impactor diameters, D_{imp}, using the crater-scaling relationships described in *Methods Sec. 5*, and assuming a mean impact speed v_{imp} = 5.2 km/s, that is appropriate for the main belt [Bottke et al. 2005]. We calculated the main belt exposure age by considering the CSFD, $N_{\mathrm{C,\,MBA}}$, of MBAs calculated from observations of the MBA size distribution and models of their collisional evolution [Bottke et al. 2005]. By numerically differentiating $N_{\mathrm{C,\,MBA}}$, we derive the incremental size frequency distribution $N_{\mathrm{I,\,MBA}}$ of MBAs with diameters D:

$$N_{\mathrm{I,\,MBA}}(D_k) = N_{\mathrm{C,\,MBA}}(\geq D_k) - N_{\mathrm{C,\,MBA}}(\geq D_{k+1}) \quad (19)$$

where k is the index of the logarithmically binned CSFD data and $D_{\mathrm{imp},k+1} > D_{\mathrm{imp},k}$. Then, the number of impacts, N_{MBA}, over a mean time interval, t_{coll}, on to a circular area on an asteroid with an area equivalent to the *Shallow Crater Region,* A_{SCR}, by an object with diameter D_{imp} is given by:

$$N_{MBA} = N_{\mathrm{I,\,MBA}}(D_{\mathrm{imp}}) \times P_i \times \frac{1}{2}\left(\frac{D_{\mathrm{imp}}}{2} + (A_{SCR}/\pi)^{1/2}\right)^2 \times t_{\mathrm{coll}} \quad (20)$$

where the third term on the right side of Eq. (20) is the collisional cross-section divided by 2, as we approximate that the *Shallow Crater Region* is shielded from half of all potential impactors by the bulk shape of Eros. We assume a constant impact probability, $P_i = 2.9 \times 10^{-18}$ km^{-2} yr^{-1} that is appropriate for the main belt [Bottke et al. 2005]. The exposure age of the *Shallow Crater Region* can then be determined by fitting the measured impactor CSFD that impacted that area to Eq. (20) and solving for t_{coll}..

The formulation presented in Eq. (20) can also be used to estimate the relative rate of impacts of a given size. In the case of the Shoemaker impact, we estimate that the impactor was on the order of ~ 270 m, for either gravity- and strength-dominated cratering. Such an impact would occur approximately every 250-750 Myr. Considering the approximately 5,000 asteroids with diameters between 10-20 km in the main belt, then production of cratering families should occur at a rate of approximately 6.7-20 per Myr. In comparison, the mean lifetime against disruption for a 5-km asteroid is approximately 4.2-6.2 Gyr. As there are approximately 30,000 5-km asteroids in the main asteroid belt, we can expect the rate of catastrophic disruption of these bodies to be approximately 4.8-7 per Myr.

For completeness, we also estimate the exposure age if Shoemaker formed after Eros dynamically decoupled from the main asteroid belt by considering the impactor flux in near-Earth space, and assuming a mean impact speed v_{imp} = 18.5 km/s. We use the cumulative impact flux determined by [Brown et al. 2002] based on observations of bolide detonations in Earth's atmosphere. The cumulative number of objects with diameters greater than Dimp colliding with Earth per year is given by Eq. (3) in [Brown et al. 2002]. We normalize this cumulative flux to the cross-sectional area of the *Shallow Crater Region* to obtain:

$$N_{\mathrm{C,NEA}}(D_{\mathrm{imp}}) = 10^{1.568} {D_{\mathrm{imp}}}^{-2.7} \times \frac{A_{SCR}/2\pi}{R_{\mathrm{Earth}}^2} \quad (21)$$

where R_{Earth} is Earth's radius. Then, the number of impacts in near-Earth space, N_{NEA}, over t_{coll} is determined by numerically integrating Eq. (21) to find:

$$N_{NEA} = N_{\mathrm{I,NEA}}(D_{\mathrm{imp}}) \times t_{\mathrm{coll}} \quad (22)$$

Data availability

MSI images and NLR data from the NEAR mission are available in the Planetary Data System Small Bodies Node hosted by the University of Maryland: https://pds-smallbodies.astro.umd.edu/data_sb/missions/near/index.shtml.

Measured dimensions and locations of craters and host boulders are available in Supplementary Information Table 1.

Code availability

The Small Body mapping tool is a publicly available mapping toolset that is available through the software's website: http://sbmt.jhuapl.edu/.

Methods Only References

56. Gaskell R. W. et al. Meteoritics & Planetary Science 43:1049–1061 (2008b)

57. Daly, R.T., et al. Geophysical Research Letters e2020GL089672 (2020).

58. Barnouin, O.S., et al. Planetary and Space Science 180, 104764 (2020).

59. Yeomans, D.K., et al. Science, Volume 289, Issue 5487, pp. 2085-2088 (2000).

60. Ballouz, R.-L., et al. Monthly Notices of the Royal Astronomical Society 485, 697-707 (2019).

61. Melosh, H.J. Impact Cratering: A Geologic Process (1989).

62. Kreyszig, E., 1993. Advanced Engineering Mathematics. Whiley, New York

63. Nishiyama, G., et al. JGR Planets 126, e2020JE006594 (2020).

64. Sato, H., Fehler, M. C., & Maeda, T. Seismic wave propagation and scattering in the heterogeneous Earth. Berlin Heidelberg: Springer Science & Business Media. (2012).

65. Daubar, I., et al. Space Science Reviews, 214(8), 1–68 (2018).

66. Dainty, A. M., et al. Seismic scattering and shallow structure of the Moon in oceanus procellarum. The Moon, 9, 11–29. (1974).

67. Virtanen, P., et al. Nature Methods, 17(3), 261-272 (2020).

68. Holsapple, K.A., and Schmidt, R.M. Journal of Geophysical Research 92, 6350 (1987).

69. Holsapple, K.A., & Housen, K.R. Icarus 191, 586–597 (2007).

Author Information:

The authors declare no competing financial interests. Correspondence and requests for materials should be addressed to R.-L.B. (ronald.ballouz@jhuapl.edu).

Supplementary Files

This is a list of supplementary files associated with this preprint. Click to download.

- SupplementaryInformationTable1BallouzEtAl2022.pdf
- ExtendedDataBallouzEtAl2022.pdf